Full length article

Enhanced energy absorption performance of 3D printed 2D auxetic lattices

Niranjan Kumar Choudhry [a], Biranchi Panda [a,*], S. Kumar [b,c,**]

[a] *Sustainable Resources for Additive Manufacturing (SreAM) Lab, Department of Mechanical Engineering, Indian Institute of Technology Guwahati, India*
[b] *James Watt School of Engineering, University of Glasgow, Glasgow G12 8QQ, UK*
[c] *Glasgow Computational Engineering Centre, University of Glasgow, Glasgow G12 8LT, UK*

ARTICLE INFO

ABSTRACT

Auxetic lattices have attracted increasing attention due to their unusual mechanical behavior and potential for an array of applications. However, a narrow window of stiffness realizable for a given cell topology limits their applications. In this study, a pair of novel 2D re-entrant auxetic lattices capable of exhibiting enhanced stiffness and energy absorption is proposed by introducing vertical ligaments into conventional re-entrant structures. These modified re-entrant auxetic lattices were realized via fused deposition additive manufacturing. The deformation patterns and the energy absorption characteristics of 3D printed auxetic lattices under quasi-static compression were investigated both via Finite Element (FE) simulations and experiments. The effective elastic stiffness of the proposed lattices was theoretically estimated. The FE results corroborated by experiments, elucidate the role of different sub-cells on the effective mechanical properties of the proposed auxetic lattices. The results indicate that the proposed structures — Type A and B variants, exhibit enhanced stiffness (+355%) and superior energy absorption (+165%) in comparison to conventional 2D re-entrant lattices of the same mass. Furthermore, the findings of the study suggest that the strength, stiffness, energy absorption capacity and Poisson's ratio of 2D auxetic lattices can be tailored by tuning the sub-cell properties and cell wall thickness.

1. Introduction

Cellular solids such as cork, wood, bone etc. are omnipresent in nature [1,2]. They are either open or closed cell structures with a periodic or stochastic arrangement of unit cell topology. They possess a desirable combination of strength and toughness properties at very low relative density. The mechanical properties of lattices (having periodic arrangements of the unit cells) can be tuned by controlling its unit cell topology [3,4] and has widespread applications in biomedical [5,6], sensing [7,8], aerospace [9], defense [9–12], automobile [13–15] industries.

Auxetic structures are a class of cellular structures that exhibit lateral expansion under tension (conversely lateral contraction under compression) and hence show negative Poisson's ratio (NPR) [16]. It has been well established that a wide range of negative Poisson's ratios can be obtained by varying the architectural parameters of the cellular geometry [17–20]. These auxetic structures when compressed, deforms with bending dominated deformation modes, leading them to capable for high energy absorption characteristics. Auxetic structures are encountered in a range of industries such as textiles, aerospace, automotive, biomedical etc. Auxetic materials/structures exhibit unusual Poisson's ratio, and energy absorption capabilities [21]. However, they exhibit relatively poor stiffness, strength and stability, due to

their geometrical configuration. Usually, these drawbacks limit their engineering applications.

In order to enhance the stiffness of 2D auxetic structures, different methodologies have been proposed by different researchers which improves the stiffness at the cost of their energy absorption capability. In the works of Sun et al. [22], multifunctional hierarchical honeycomb (MHH) structures were proposed where the solid walls of the structure were replaced by two different types of NPR honeycombs having equal masses; named as anisotropic re-entrant honeycomb and isotropic chiral honeycomb. The MHH structure showed significant improvement in Young's modulus, and it can be tuned by changing the geometrical parameters of the NPR honeycombs. A similar work has been done by Rayneau et al. [23], where hierarchical substructure has been added into a coarse auxetic lattice to realize ultra-lightweight structures possessing high stiffness and strength.

The addition of ligaments within the 2D auxetic can improve the stiffness of structure. Zied et al. [24] proposed two new designs (splined and stiffened re-entrant honeycomb structures) to further improve stiffness of the re-entrant honeycomb structure. The splined re-entrant structure stiffness was improved by adding a horizontal link to the inclined ligaments, and named as stiffened re-entrant honeycomb structures. Similarly, Lu et al. [25] reported improved stiffness by adding narrow rib into a regular re-entrant structure. Chen et al. [26] modified

the re-entrant honeycomb structure by adding horizontal and vertical ribs. The vertical ribs are parallel to the loading direction. They found that the Poisson's ratio of the structures quadratically varies with relative density while Young's modulus has linear relationship with relative density. The stiffness along the stiffening direction was improved by 200% and such improvement was obtained while sacrificing the negative Poisson's ratio property.

Researchers also attempted to improve the stiffness of 2D auxetic structure by embedding different unit cells to form hybrid structures. Fu et al. [27,28] embedded a rhombic configuration into a re-entrant honeycomb to design a new structure. Improved stiffness was observed at higher axial stiffness of reinforcing walls. Further, Zhang et al. [29] proposed two novel ways to make a hybrid structure from auxetic re-entrant and missing rib structures. In the first methodology, an anti-tetrachiral structure was added with a missing rib (cross-chiral) configuration, while in the second methodology a variable cross-chiral structure was added with a square missing rib structure. The effective stiffness of proposed structures was higher than cross-missing rib structures and can be tailored by changing geometrical parameters. Similarly, A Ingrole et al. [30] proposed two hybrid designs by stacking regular honeycomb with auxetic-strut unit cells.

Numerous studies show that cellular structures deform under compression either in bending- or stretching-dominated mode. It has been found that the stretching-dominated structures mostly possess higher elastic modulus and initial peak stress (yield stress) than that of bending-dominated structures for the same relative density, while exhibiting a soft post-yield response which leads to lower energy absorption [31]. On the other hand, bending-dominated structures show higher energy absorption but lower elastic modulus and initial peak stress (yield stress). In the first two methods (i.e. formation of hierarchical structures, and ligament addition), due to higher node connectivity, cellular structures exhibited stretching-dominated deformation which resulted in an increase in stiffness [32,33] at the cost of energy absorption capacity. On the other hand, in a hybrid structure, there is an improvement in energy absorption characteristics with a marginal improvement in stiffness (except in some cases where a decrease in energy absorption performance was observed [30]) due to localized deformation. The deformation of a hybrid structure is controlled by their embedded unit cells having the same or different strut thickness, which further leads to bending-dominated deformation.

It is clear from the above review that researchers have proposed new auxetic designs that can improve the stiffness of the structure at the expense of energy absorption capability. Nonetheless, a very few studies focused on simultaneous improvement of both the properties. This gap set the stage for the present work. In this study, conventional re-entrant auxetic lattice was modified and two new designs namely, Type-A and B variants were proposed. The design modification includes selective addition of vertical ligaments to the conventional structure that resulted in enhanced stiffness and energy absorption without significantly altering relative density of the structure. The geometrical configurations of the proposed structures are described in Section 2.1. Based on the Castigliano's second theorem, theoretical formulae for the effective elastic constants of the structures are presented in Section 2.2. In Section 3, fabrication methodology, experimental testing, and the details of the Finite Element (FE) analysis are described. The FE model validation and discussion on strength, stiffness, energy absorption performance and Poisson's ratio of the proposed structures can be found in Section 4. In parametric analysis section, the effect of vertical strut thickness on strength, stiffness, and energy absorption capacity are discussed. Finally, conclusions from this study and future research prospects are given in Section 5.

2. Novel auxetic lattices with vertical ligaments

2.1. Unit cell design

As mentioned previously, two new unit cells (Type-A and Type-B variants) were designed by adding vertical ligaments to the re-entrant

honeycomb structure (Modified RH), described in the previous work of the authors [34], as depicted in Fig. 1. The vertical ligaments are added to nodes or joints with higher node connectivity, while the lower node connecting joints remain unchanged. The presence of a low rotational stiffness joint allows easy rotation of inclined ligaments about the joint that enables higher compaction of deforming layers leading to increase in onset of densification strain and therefore, the vertical ligament is added only at higher node connectivity joints (see Fig. 1(b)). The design parameters of modified RH, Type-A and Type-B variants are summarized in Table 1. Table 2 shows the theoretical relative density of these two proposed structures obtained by unit cell analysis while neglecting the node size.

2.2. Analytical prediction of effective Young's modulus using the energy method

The energy method is employed to determine the elastic modulus of the auxetic lattices within the purview of linear elastostatics. To find out the expression for the average elastic modulus in the y direction (E_y), a compressive stress σ_y is applied to the structure as shown in Fig. 2(a). Note that vertical ligaments of the unit cell only experience the axial load. Fig. 2(b) represents the free-body diagram (FBD) of the unit cell, where F_1 and F_2 are the axial loads in the vertical member h and h_0 respectively. The sum of all forces in the Y direction for the whole unit cell must be equal to F (Eq. (1)), i.e.

$$F_1 + F_2 = F \tag{1}$$

where F is the total force acting on the unit cell due to applied compressive stress σ_y. Out-of-plane thickness of the structure is assumed to be unity. Hence, the expression for F can be written as (Eq. (2))

$$F = 2\sigma_y \left(l_1 \cos \Theta_1 - l_2 \cos (\Theta_1 + \Theta_2) \right) \tag{2}$$

The analysis is further simplified by considering one-fourth of the unit cell i.e the part **abcde** (Fig. 2(c)). The inclined member **bc** and **cd** are subjected to both axial (F_{bc}^n and F_{cd}^n respectively) and transverse loads (F_{bc}^t and F_{cd}^t respectively) which are determined by considering equilibrium of forces and method of joints (Fig. 2(c)). The expressions for axial and transverse loads (Eqs. (3) to (6)) are as follows

$$F_{bc}^n = \frac{F_1 \sin (\Theta_1 + \Theta_2)}{2} \tag{3}$$

$$F_{bc}^t = \frac{F_1 \cos (\Theta_1 + \Theta_2)}{2} \tag{4}$$

$$F_{cd}^n = \frac{F_1 \sin (\Theta_1)}{2} \tag{5}$$

$$F_{bc}^t = \frac{F_1 \cos (\Theta_1)}{2} \tag{6}$$

After computing the forces in different ligaments/members, the energy method is used to derive the expression for the stiffness of the lattice structure. Axial, bending and shear deformations are considered in the strain energy calculation, while strain energy due to torsion is ignored. The total strain energy stored in one-fourth of the unit cell is expressed as (Eq. (7)):

$$U = \frac{1}{2} \int_0^{\frac{h}{2}} \frac{\left(\frac{F_1}{2} \right)^2}{\left(\frac{t}{2} \right) E_s} dx + \frac{1}{2} \int_0^{l_2} \frac{\left(\frac{F_1 \sin(\Theta_1 + \Theta_2)}{2} \right)^2}{t E_s} dx$$

$$+ \frac{1}{2} \int_0^{l_2} \frac{\left(\frac{F_1 \cos(\Theta_1 + \Theta_2)x}{2} \right)^2}{I_{bc} E_s} dx + \frac{1}{2} \int_0^{l_2} \frac{\left(\frac{F_1 \cos(\Theta_1 + \Theta_2)}{2} \right)^2}{t k G_s} dx$$

$$+ \frac{1}{2} \int_0^{l_1} \frac{\left(\frac{F_1 \sin(\Theta_1)}{2} \right)^2}{t E_s} dx + \frac{1}{2} \int_0^{l_1} \frac{\left(\frac{F_1 \cos(\Theta_1)x}{2} \right)^2}{I_{cd} E_s} dx$$
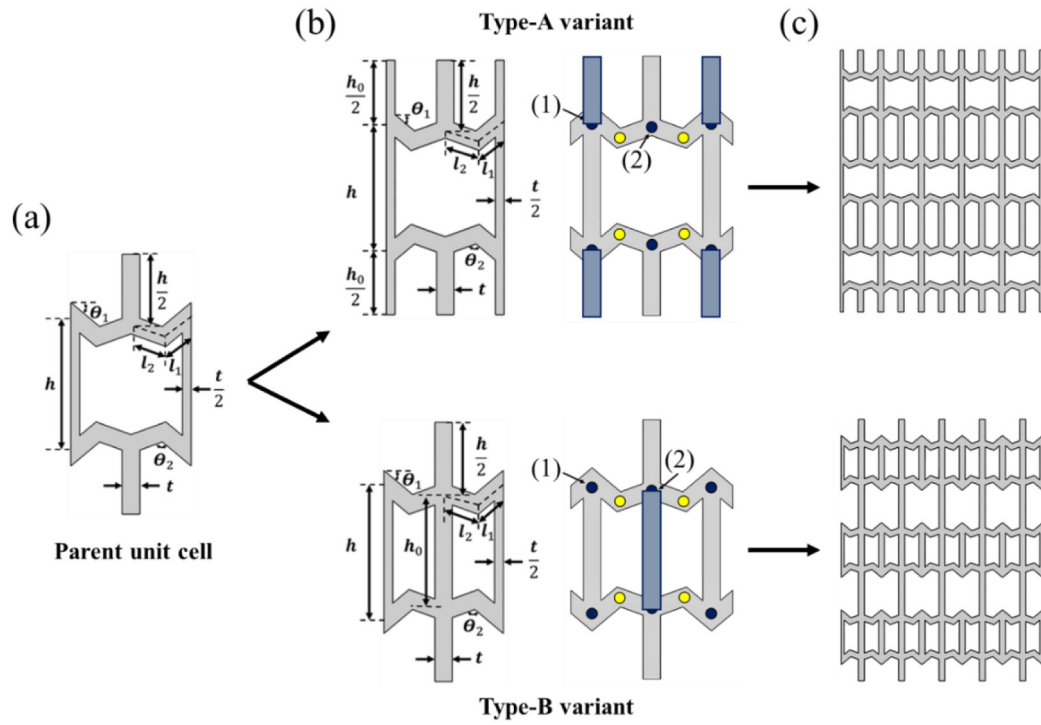
Fig. 1. (a) Unit cell topology of modified RH [34] (b) Type-A variant and Type-B variant unit cell topology (black dots represent nodes with higher connectivity; yellow dots represent nodes with lower connectivity; blue ligaments are added to the joints) and (c) 2D Type-A and Type-B lattices. (For interpretation of the references to colour in this figure legend, the reader is referred to the web version of this article.)
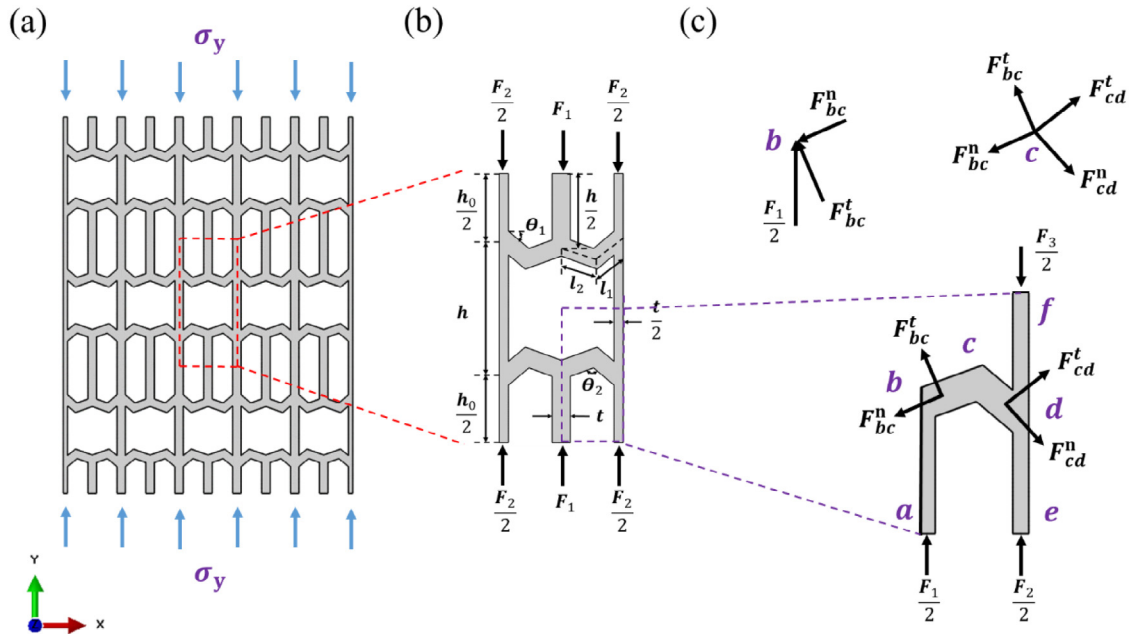

Fig. 2. Schematic representation of (a). 2D lattice structure of type-A variant under Y direction far-field compressive loading, (b). FBD of unit cell of type-A variant and (c). force experienced by different members of the unit cell and FBD of joints **b** and **c**.

Table 1
Architectural parameters of auxetic structures.

Structure	h (mm)	h_0 (mm)	l_1 (mm)	l_2 (mm)	t (mm)	θ_1 (°)	θ_2 (°)	$\bar{\rho}$
Modified RH	16	–	4	4	2	40	120	0.310
Type-A variant	16	10.98	4	4	2	40	120	0.349
Type-B variant	16	13.59	4	4	2	40	120	0.346

Table 2
The formulae for the relative density of Type-A and B auxetic structures.

Auxetic structure	Relative density ($\bar{\rho}$)
Type-A variant	$\bar{\rho} = \dfrac{\left(\left(h + \frac{h_0}{2}\right) + 2(l_1 + l_2)\right)t}{(h + h_0)\left(l_1 \cos\theta_1 - l_2 \cos(\theta_1 + \theta_2)\right)}$
Type-B variant	$\bar{\rho} = \dfrac{\left(\left(h + \frac{h_0}{2}\right) + 2(l_1 + l_2)\right)t}{(h + h_0)\left(l_1 \cos\theta_1 - l_2 \cos(\theta_1 + \theta_2)\right)}$

$$+ \frac{1}{2}\int_0^{l_1} \frac{\left(\frac{F_1 \cos(\Theta_1)}{2}\right)^2}{tkG_s}dx + \frac{1}{2}\int_0^{\frac{h_0}{2}} \frac{\left(\frac{F_2}{2}\right)^2}{\left(\frac{t}{2}\right)E_s}dx$$

$$+ \frac{1}{2}\int_0^{\frac{h}{2}} \frac{\left(\frac{F_3}{2}\right)^2}{\left(\frac{t}{2}\right)E_s}dx \tag{7}$$

where E_s is the elastic modulus and G_s is the shear modulus of the base material and k is the shear correction factor (a value of 0.83 is chosen for rectangular cross-section) which accounts for non-uniformity of shear strain within the ligament, [35]. I_{bc} and I_{cd} are moments of inertia of inclined member **bc** and **cd** respectively. As both inclined members have the same cross-sectional area, they have the same moment of inertia ($I_{bc} = I_{cd} = \frac{t^3}{12}$). Castigliano's second theorem is employed to find out the displacement of points. Hence total displacement (δ_y) of one-fourth part of the unit cell in the y direction with respect to **8** (considering $\delta_a = \frac{\partial U}{\partial\left(\frac{F_1}{2}\right)} = 0$) is expressed as (Eqs. (8) & (9)):

$$\delta_y = \delta_f - \delta_a \tag{8}$$

where δ_f and δ_a are the displacements of points **f** and **a** in the y direction respectively.

$$\delta_y = \frac{\partial U}{\partial\left(\frac{F_3}{2}\right)} = \frac{\left(4nh_0^2 + 4h(n + h_0)^2 + h_0(n - h_0)^2\right)F}{8tE_s(n + h_0)^2} \tag{9}$$

where

$$n = \left(h + l_1 \sin^2\Theta_1 + 3.24l_1 \cos^2\Theta_1 + \frac{4l_1^3 \cos^2\Theta_1}{t^2} + l_2 \sin^2(\Theta_1 + \Theta_2)\right.$$

$$\left. + 3.24l_2 \cos^2(\Theta_1 + \Theta_2) + \frac{4l_2^3 \cos^2(\Theta_1 + \Theta_2)}{t^2}\right)$$

Now, average strain in y direction, ε_y is obtained as (Eq. (10)):

$$\varepsilon_y = \frac{\delta_y}{\left(\frac{h + h_0}{2}\right)} \tag{10}$$

where, $\left(\frac{h + h_0}{2}\right)$ is the initial vertical distance between points **a** and **f**. Young's modulus for variant- A $\left(E_y^A\right)$ can be expressed as (Eq. (11)):

$$E_y^A = \left(\frac{2t(h + h_0)(n + h_0)^2}{(l_1 \cos\Theta_1 - l_2 \cos(\Theta_1 + \Theta_2))\left(4nh_0^2 + 4h(n + h_0)^2 + h_0(n - h_0)^2\right)}\right)E_s \tag{11}$$

A similar approach is used to estimate Young's modulus of variant-B $\left(E_y^B\right)$, and can be expressed as (Eq. (12)):

$$E_y^B = \left(\frac{2t(h + h_0)(n + h_0)^2}{(l_1 \cos\Theta_1 - l_2 \cos(\Theta_1 + \Theta_2))\left(nh_0^2 + 4h(n + h_0)^2 + h_0(2n + h_0)^2\right)}\right)E_s \tag{12}$$

3. Experimental and numerical methods

3.1. Additive manufacturing via FDM 3D printing

The proposed auxetic structures were fabricated using a Fused Deposition Modeling (FDM) printer (AEQON 400 V3 make of DIVIDE BY ZERO). Filament of Acrylonitrile Butadiene Styrene (ABS) material with 1.75 mm diameter was used to print the samples using 0.6 mm diameter nozzle. In principle, structures can be printed in X or Y or Z direction. However, "Z" direction was chosen as the build direction in this study to minimize the time required for printing the structure (Fig. 3(a)). Samples were printed at a speed of 30 mm/s with 100% infill density and 0.2 mm layer thickness. To minimize anisotropy, a raster angle of $\pm 45^0$ was chosen. Bed and extruder temperatures of the printer were maintained at 90 °C and 240 °C respectively. The proposed 3D printed structures (Type-A and Type-B variants) are shown in Fig. 3(b).

3.2. Quasi-static compression tests

The crushing response of 3D printed auxetic structures was evaluated via quasi static compression tests using 250 kN UTM (MEDIAN 250) at room temperature. Fig. S1 shows the experimental setup used for the quasi-static compression test (refer to supplementary information (S1) for more details). Samples were held in between the top and bottom platens. The top platen was connected to the load cell (with an accuracy of $\leq \pm 1\%$) mounted on the crosshead. The crosshead is mounted on the column, and its position was fixed before loading the sample. In the current set up, the top platen was fixed and movement was given to the bottom platen at a displacement rate of 2 mm/min [36]. This corresponds to an average strain rate of 0.00037037 s^{-1}.

High magnification videos were recorded using Sony NXCAM video camera to understand deformation behavior of the structures. The load–displacement response was recorded. Three samples for each structure were tested, and their average load–displacement response was used for further analysis. The compressive stress (σ) and strain (ε) were calculated from the load–displacement response using Eqs. (13) and (14) respectively.

$$\sigma = \frac{F}{W \times L} \tag{13}$$

$$\varepsilon = \frac{\delta}{H} \tag{14}$$

where δ is the displacement due to applied compressive load F ; H, W and L are the height, width and thickness (out of plane) of the structure respectively.

3.3. Finite element (FE) analysis

For systematically analyzing the quasi-static compression response of 3D printed auxetic structures, FE analysis was conducted using a commercial FE package (ABAQUS) with a nonlinear explicit solver. Discrete rigid elements were assigned for top and bottom platens to simulate the moving and stationary platens, respectively. The top platen was given downward motion by allowing a single degree of freedom while all degrees of freedom for the bottom platen was constrained. Fig. 4 shows a typical FE mesh of the Type-A variant with appropriate loading and boundary conditions. The details of the tensile and compressive behavior of bulk parent material are given in the supplementary information (S2).

The Linear Drucker–Prager plasticity model along with the Ductile-damage failure criterion (Angle of Friction (β) = 12 degree, Flow Stress Ratio = 0.82 and Dilation Angle (ψ) = 12 degree) was employed to simulate the crushing behavior of auxetic lattices under quasi-static compression (refer to supplementary information (S3) for more details) [34]. Ductile-damage model captures the fracture and failure of
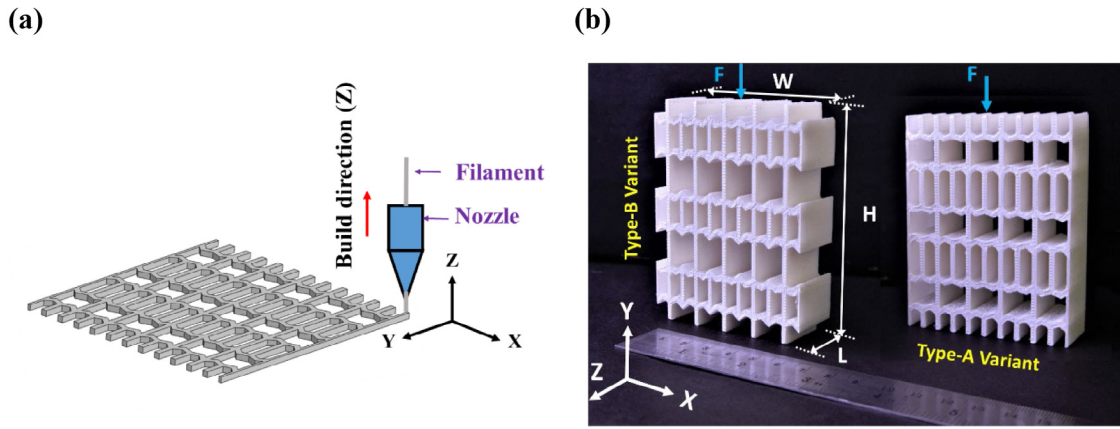
Fig. 3. (a) Schematic diagram of FDM printing process and (b) 3D printed Type-A and Type-B 2D lattice structures.
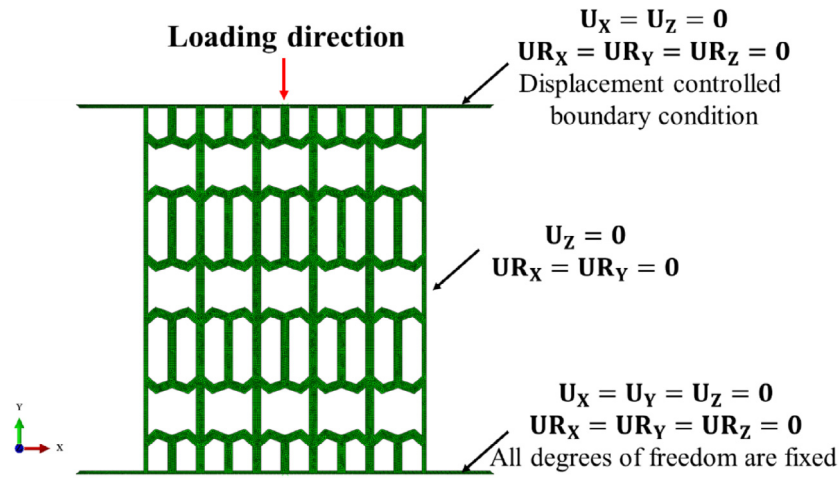

Fig. 4. A typical FE mesh of Type-A variant structure with appropriate loading and boundary conditions for numerical modeling of quasi-static compression tests.

the struts; a fracture strain factor of 0.008, a stress triaxiality factor of 0.33 and a strain rate of 0.00133 s^{-1} were considered. A 'general contact interaction' was utilized for all the surfaces, where "hard" contact was used for the normal interaction and a friction coefficient of 0.3 was assigned for tangential behavior. A mesh convergence test was performed to select the optimal mesh size (refer to supplementary information (S4) for more details). An 8-node hexahedral (C3D8R) 3D solid element with a mesh size of 0.25 mm was used with enhanced hourglass control and second-order accuracy consideration [37].

4. Results and discussion

4.1. Numerical model validation

Fig. 5 shows stress–strain response of the structures obtained from FE analysis and experiment. A good agreement between FE and experimental results was found during elastic deformation. The discrepancy in post–yield response can be ascribed to the cracks (supplementary information: S5) observed in 3D printed structures at some locations in the vertical struts during the early stages of deformation.

In the Type-A variant, deviation in the stress value was observed around 0.017 strain where the stress falls sharply due to cracking and it was confirmed by the deformation map (see Fig. 5(a)). It is clear from the FE deformation map that the high-stress concentration zones form near the joint at the deformed row corners (row at center) but fractures were not observed near any joints. However, in the experimental studies, micro pores were found in ligaments and one of the

ligaments on the outermost right-hand side fractured (see Fig. 5(a)) and delaminated which leads to deviation in the results. Similar behavior was also observed for Type-B variant structure (Fig. 5(b)). Optical images captured at different locations within the structures are shown in fig. S4 (supplementary information: S5). Similar issues associated with pores present in FDM printed structures were reported in [38–40]. This process induced defects were not incorporated in this FE model. These defects could be minimized to some extent by optimizing the process parameters but to capture the localized failure of lattices accurately owing to localized triaxial stress-state, failure strain with respect to the stress triaxiality ought to be considered [41] and is left to a subsequent study. Nevertheless, due to similar deformation patterns obtained from experimental and FE studies, the FE model is used for further analysis.

Young's modulus and yield stress predicted by the FE model were also found to be consistent with experimental results. The maximum deviation between experimental and FE results for Young's modulus and yield stress was 6.14% and 7.26% respectively.

4.2. Young's modulus, yield strength and compressive strength

The Young's modulus of the Type A and B variants obtained by experimental testing, FEA, and theoretical models are summarized in Table 3. For both Type A and B variants, the theoretically predicted results were closer to the FE results. It was noted from experimental results (Table 3) that the Type-A variant showed the highest elastic modulus (384.73 MPa) followed by the Type-B variant (251.98 MPa).
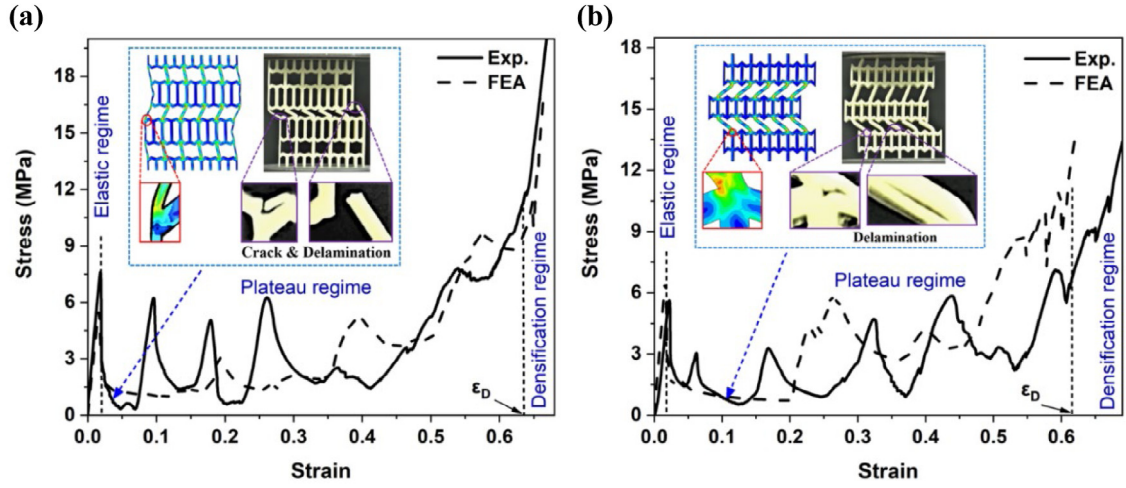
Fig. 5. Experimental vs. predicted stress–strain response of (a) Type-A and (b) Type-B variant auxetic structures (arrow indicates onset strain of delamination).
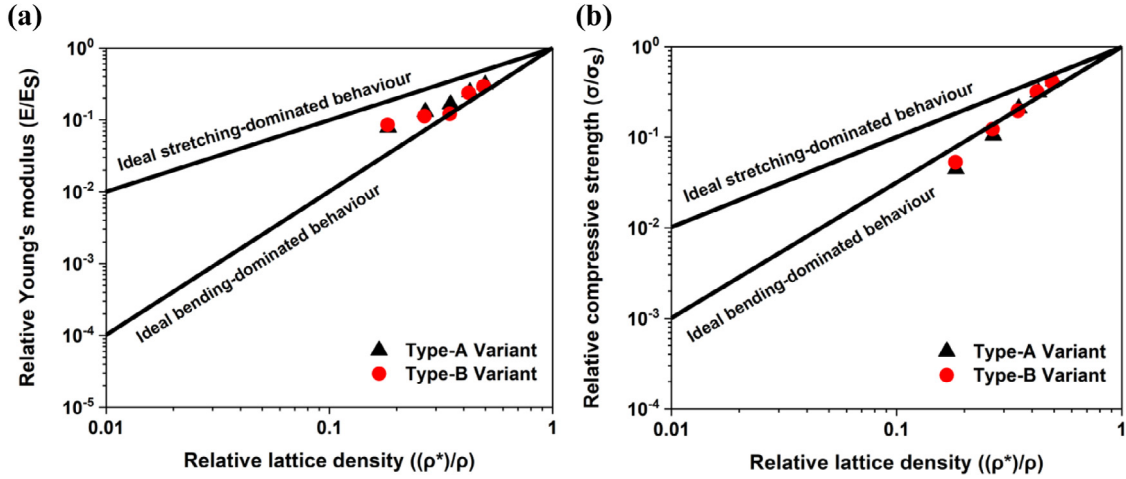

Fig. 6. Plot for (a) relative Young's modulus and (b) relative compressive strength (Solid lines represent ideal stretching and bending-dominated behavior).

Table 3
Comparison of Young's modulus of the Type A and B variant structures.

Properties	Type-A variant			Type-B variant		
	FEA	Exp.	Theoretical	FEA	Exp.	Theoretical
Young's modulus (MPa)	362.53	384.73	379.74	266.73	251.98	272.59

The 355% and 198% improvements in Young's modulus of Type-A and Type-B structures respectively in comparison to 'modified-RH' is due to their composite architecture with two sub-cells indicated as 'cell -1' and 'cell-2' (see Fig. S5). Like composite materials, the performance of lattice structure depends on their constitutive sub-cell properties and therefore, "rule of mixture" was used to estimate the overall stiffness of the structures (see supplementary information; S6). The rule of mixture is a theoretical model widely used for the estimation of the Young's modulus of the composite materials based on the volume fractions of constituent phases. In this study, the sub-cell properties were obtained using the theoretical expression (Section 2.2). The predicted elastic moduli values using the volume fractions of sub-cells, show good agreement within the upper and lower bound curves of the composite rule of mixture (Table S5).

Fig. 6(a) and (b) show the scaling relation between macroscopic properties such as Young's modulus and compressive strength and the relative density for Type-A and Type-B variants. As per the Ashby

model [1,42], approximated relation for open-cell cellular structures for relative Young's modulus and relative compressive strength to relative lattice density are given by Eqs. (15) and (16) respectively.

$$\frac{E}{E_S} = C_1 \left(\frac{\rho^*}{\rho} \right)^m \tag{15}$$

$$\frac{\sigma}{\sigma_S} = C_2 \left(\frac{\rho^*}{\rho} \right)^n \tag{16}$$

where E and E_S are Young's moduli and σ and σ_S are the yield strengths of the cellular structure and its base material respectively, while ρ^* and ρ are the densities of cellular structure and its base material respectively. C_1 and C_2 are constants of proportionality and m and n are the exponents of the Ashby model.

Eq. (15) is used to obtain the scaling relation between Young's modulus and the relative density for Type-A and Type-B variant structures, and the value of the geometric constant of proportionality C_1 and exponent m are obtained through curve fitting of relative modulus data
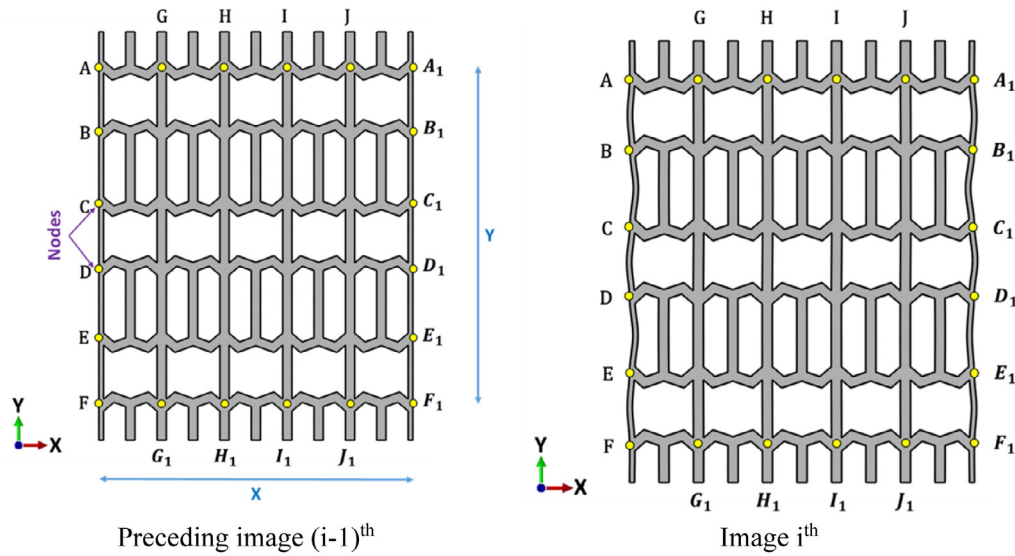
Fig. 7. Schematic representation of images for calculation of average longitudinal and transverse distance.

Table 4
Comparison of Yield and compressive strengths of auxetic lattices.

Structure	Yield strength (MPa)			Compressive strength (MPa)		
	Exp.	FEA	Error (%)	Exp.	FEA	Error (%)
RH	2.77	2.71	−2.21	2.85	2.92	2.39
Modified-RH	3.3	3.18	−3.77	3.27	3.46	5.49
Type-A variant	7.62	6.48	−3.25	7.85	8.97	12.48
Type-B variant	5.62	6.06	7.26	7.25	8.56	15.31

obtained for various relative densities (see supplementary information: S7 and Table 5). The geometric constant of proportionality C_1 for the Type-A variant and Type-B variant structures is in the range of 0.683 to 0.835 and 0.443 to 0.879 respectively, while exponent m is in the range of 1.26 to 1.43 and 0.96 to 1.54 respectively. The value of C_2 and n were found using similar method. The geometric constant of proportionality C_2 for the Type-A variant and Type-B variant structures are in the range of 0.683 to 0.835 and 0.443 to 0.879 respectively, while exponent n is in the range of 1.26 to 1.43 and 0.96 to 1.54 respectively. It can be concluded that both relations follow positive power law.

As per the Gibson–Ashby model, the value of fitting exponent m (for Young's modulus) is 1 for stretch-dominated structures and 2 for bending-dominated structures, while fitting exponent n (for yield strength) is 1 and 1.5 for stretch-dominated and bending-dominated structures respectively [43,44]. The fitting exponent m for both structures is in the range of 1 to 2 (see Fig. 6(a)). It can be noted from Fig. 6(a) that at lower relative density, the deformation of the structure is bending-dominated and as relative density increases its degree is reduced. Further, Type-B variant has the largest m values for each relative density and hence shows more bending-dominated deformation behavior than that of Type-A. This confirms the enhanced stiffness is mainly attributed to the fact that the deformation mode is changing from more bending-dominated to less bending-dominated mode.

Table 4 presents the comparative analysis of yield strength and compressive strength of all structures with conventional RH structure. The compressive strength of a lattice structure is the maximum stress (σ_P) a structure can resist before densification. Fig. 6(b) shows the relative compressive strength as a function of relative density for all structures. The fitting exponent n for both variants is higher than 1.5. At low relative densities, the values of fitting exponent n reach a value of 2.347 and 2.13 for Type-A and Type-B variants respectively,

and hence they exhibit bending-dominated deformation at lower relative density. As relative density increases, the influence of bending reduces. Type-B variant outperforms the Type-A variant in terms of compressive strength as it is highly anisotropic. It should be noted that isotropic structures deform and fail due to elastic buckling [42], which is responsible for lower stiffness and strength while anisotropic structures deform due to the presence of vertical pillars (parallel to loading direction) as these pillars directly carry the compressive loads from top to bottom (entire length) of the structures leading to improved stiffness and strength of the structure.

4.3. Poisson's ratio

Poisson's ratio (ν) deals with a material's distortion when it is subjected to a mechanical load. It is used to compare the structural performance of different materials (for both homogeneous and non-homogeneous) when they are elastically strained. It is the ratio of transverse (ε_t) to longitudinal strain (ε_l) (see, Eq. (17)). However, a series of deformed images captured at different instants during loading were used to calculate the Poisson's ratio (ν) as a function of imposed strain (Eq. (18)).

$$\nu = -\frac{\varepsilon_t}{\varepsilon_l} \tag{17}$$

Poisson's ratio for all the structures was calculated from the FE results. A series of deformed images were taken for a given structure and an instantaneous change in displacement of traced nodes along the transverse and longitudinal direction was calculated. The longitudinal distance (Y) was the average distance of marked nodes between the top and bottom rows while the transverse distance (X) was the average distance of marked nodes between the left and right rows. The true longitudinal ($\varepsilon_{l\ true}$) and true transverse ($\varepsilon_{t\ true}$) strains were determined for the ith image, where preceding image ($i-1$)th was considered as reference. The Poisson's ratio (ν_{yx}) [45] for the loading direction Y was calculated from below Eq. (18).

$$\nu_{yx} = -\frac{\varepsilon_{t\ true}}{\varepsilon_{l\ true}} \tag{18}$$

Here, the method used for finding the true transverse ($\varepsilon_{t\ true}$) strain is demonstrated and a similar method can be used to find the true longitudinal ($\varepsilon_{l\ true}$) strain.

Firstly, the average distance of marked nodes between the left and right rows for ith image and preceding image ($i-1$)th was calculated (Eqs. (19) and (20)) [46]. Fig. 7 shows a schematic representation

Table 5
Influence of thickness variation on Young's modulus and yield strength.

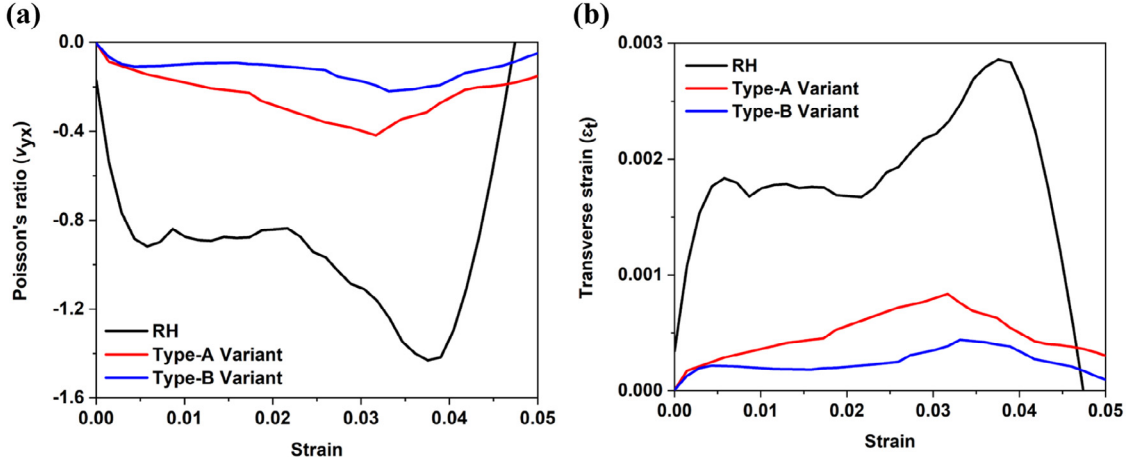| t (mm)	Type-A variant			Type-B variant		
	$\bar{\rho}$	Young's modulus (MPa)	Yield strength (MPa)	$\bar{\rho}$	Young's modulus (MPa)	Yield strength (MPa)
1	0.18	173.08	1.38	0.18	188.72	1.64
1.5	0.27	285.66	3.25	0.27	247.13	3.79
2	0.35	362.53	6.48	0.35	266.73	6.06
2.5	0.43	534.51	9.70	0.42	524.21	9.88
3	0.50	680.63	12.97	0.49	644.82	12.65

Fig. 8. (a) Poisson's ratio versus strain of test specimens and (b) corresponding transverse strain.

of images for the calculation of average longitudinal and transverse distance.

$$X_i = \frac{AA_1 + BB_1 + CC_1 + DD_1 + EE_1 + FF_1}{6} \tag{19}$$

$$X_{i-1} = \frac{AA_1 + BB_1 + CC_1 + DD_1 + EE_1 + FF_1}{6} \tag{20}$$

where, X_i and X_{i-1} are the average distance of marked nodes between the left and right rows for ith image and its preceding image (i−1)th respectively. The transverse displacement (ΔX) can be find out by using Eq. (21), and finally the true transverse ($\varepsilon_{t\ true}$) strain was calculated by following Eq. (22) [45].

$$\Delta X = X_i - X_{i-1} \tag{21}$$

$$\varepsilon_{t\ true} = \frac{\Delta X}{X_{i-1}} \tag{22}$$

Fig. 8(a) shows Poisson's ratio versus strain relationship of specimens compressed quasi-statically along Y-direction. A similar variation in Poisson's ratio was observed for the RH, Type-A and Type-B variants. In the early stages of loading, their NPR increases and becomes maximum, thereafter, further compression causes a decrease in the NPR.

The RH structure showed the highest auxeticity compared to that of the Type-A and Type-B variants with a Poisson's ratio of −1.324, −0.121 and −0.057 respectively as the inclined wall of RH-structure moved easily inwards due to applied load leading to more transverse strain (Fig. 8(b)). However, due to the presence of vertical strut in Type-A and Type-B variants, the inward movement of inclined wall is restricted which lowers the transverse strain (Fig. 8(b)). The difference in auxeticity of RH-structure, Type-A and Type-B variants is mainly due to their geometry, as Poisson's ratio is geometry dependent parameter [28,47]. The RH structure showed highest auxeticity compared to Type-A and Type-B variants and hence it is more compressible than Type-A and Type-B variants.

4.4. Energy absorption characteristics

4.4.1. Stress–strain response and deformation mechanism

Fig. 9 shows stress–strain curve and sequential deformation images of Type-A and B structures. Point-1 is taken within the elastic regime to observe the auxeticity of the structures. It can be seen from the deformation sequence (Fig. 9(b) and (d)) that both the structures contracted laterally resulting in NPR at point-1. Initially, the vertical walls of the structures only experienced axial loading, while inclined walls experienced both bending and axial loading due to which the inclined walls moved inward and the structure showed NPR.

For both the structures, initially, there is a linear increase in stress, as the cells of the structure deformed uniformly and elastically due to the instant stress distribution throughout the structure [48]. After reaching a maximum value, the stress dropped as plastic deformation started within the first layer of the structure and continuously decreases till the first layer completely collapsed. The point after which stress started dropping is marked as yield point (point-2) in both the structures. After the yield point, the deformation of structures was controlled by the sub-cell behavior. Since the low relative density sub-cell is weaker than high relative density (Table 5), initially the low relative density sub-cells were collapsed (point-3 & 4). The cells near the top and bottom plates encounter frictional resistance arising from contacting surfaces and leads to in-plane buckling of the structures (point-2). The sub-cell having lower relative density and away from the top and bottom plates is more unstable, deformed first (point-2 & 3). Thereafter, deformation moved to the other lower relative density cells, near to the top and bottom plates (as per their stability, point-4, Type-A variant). Once all the lower relative density sub-cells were deformed, the deformation wave moved to the higher relative density sub-cells (point-5 & 6) and continued till all the cells got collapsed.

A fall in the stress was observed during the deformation of one unstable layer (sub cell), and it continued till complete layer deformed. Due to complete deformation of the layer, the stability of complete structure further increases, resisting more load (a sharp increase in
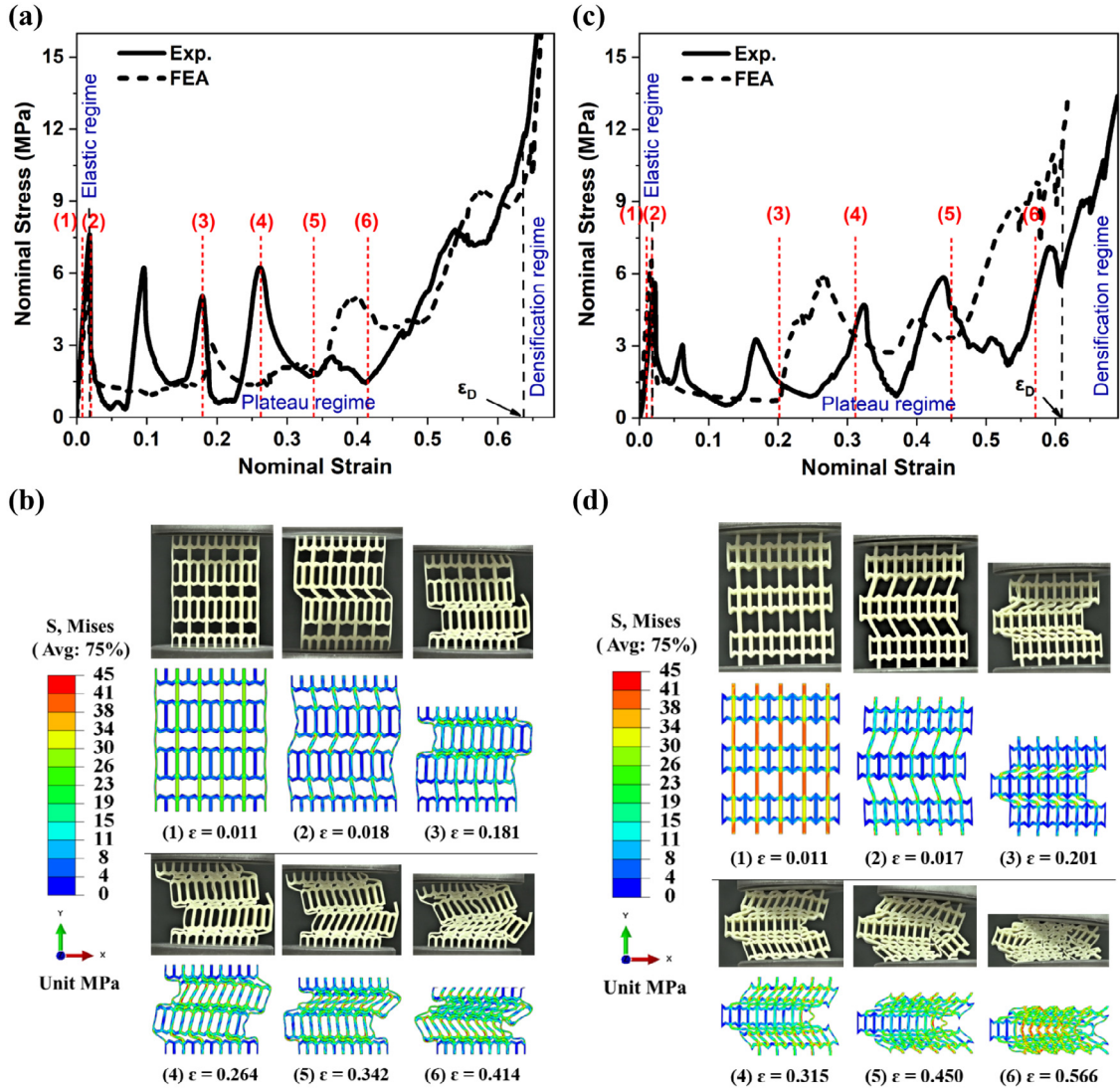
Fig. 9. Comparative analysis of auxetic structures: (a) stress–strain curve of Type-A variant (b) sequential deformation maps of Type-A variant (c) stress–strain curve of Type-B variant and (d) sequential deformation maps of Type-B variant.

stress) till another layer becomes unstable. This cyclic behavior of stress (increasing and decreasing) continues till all the rows were collapsed. Finally, densification started and after the densification, compaction of layers continues resulting rapid increase in the stress value.

4.4.2. Energy absorption performance

The energy absorption (EA) capacity and energy absorption efficiency (η) of a cellular structure are calculated up to the densification strain ε_D. Eqs. (23) and (24) were used to calculate the energy absorption capacity (MJ/m^3) and energy absorption efficiency for all auxetic structures respectively [49,50].

$$EA = \int_0^{\varepsilon_D} \sigma(\varepsilon)\,d\varepsilon \tag{23}$$

$$\eta = \frac{1}{\sigma_P} \int_0^{\varepsilon_D} \sigma(\varepsilon)\,d\varepsilon \tag{24}$$

where σ is axial compressive stress developed during compression and strain ε is its work conjugate. While σ_P is the peak stress and ε_D is the densification strain of the cellular structures. Onset of densification in lattices can be identified by three different ways [51]. In case, a sharp increase in stress is not observed at the onset of densification,

it is identified by drawing a perpendicular line from maximum stress and the corresponding intersecting strain is considered as 'onset of densification strain'.

The energy absorption capacities of the structures are indicated by the hatched area under the stress–strain curve in Fig. 10 and it is clear that the energy absorption efficiency (red color) of the structures increases with strain and attains maximum at densification strain.

The comparisons of energy absorption capacities of RH, Modified-RH, Type-A and Type-B variant structures under quasi-static compression are presented in Fig. 11(a). Initially, for all the structures, the EA curves coincide and vary linearly with lower slope up to strain value 0.2, which suggests low energy absorption capacity of the structures at lower strain. Type-A structure has slightly improved energy absorption at 0.2 strain. Further increase in strain leads to higher energy absorption of the structures with different rates. The energy absorption of the Type-A variant is the highest among all four structures. Table 6 shows a comparison of energy absorption capacity and energy absorption efficiency of all structures obtained both from experiments and FEA.

The specific energy absorption (SEA) was used to compare the structural performance which is defined as the ratio of EA of the
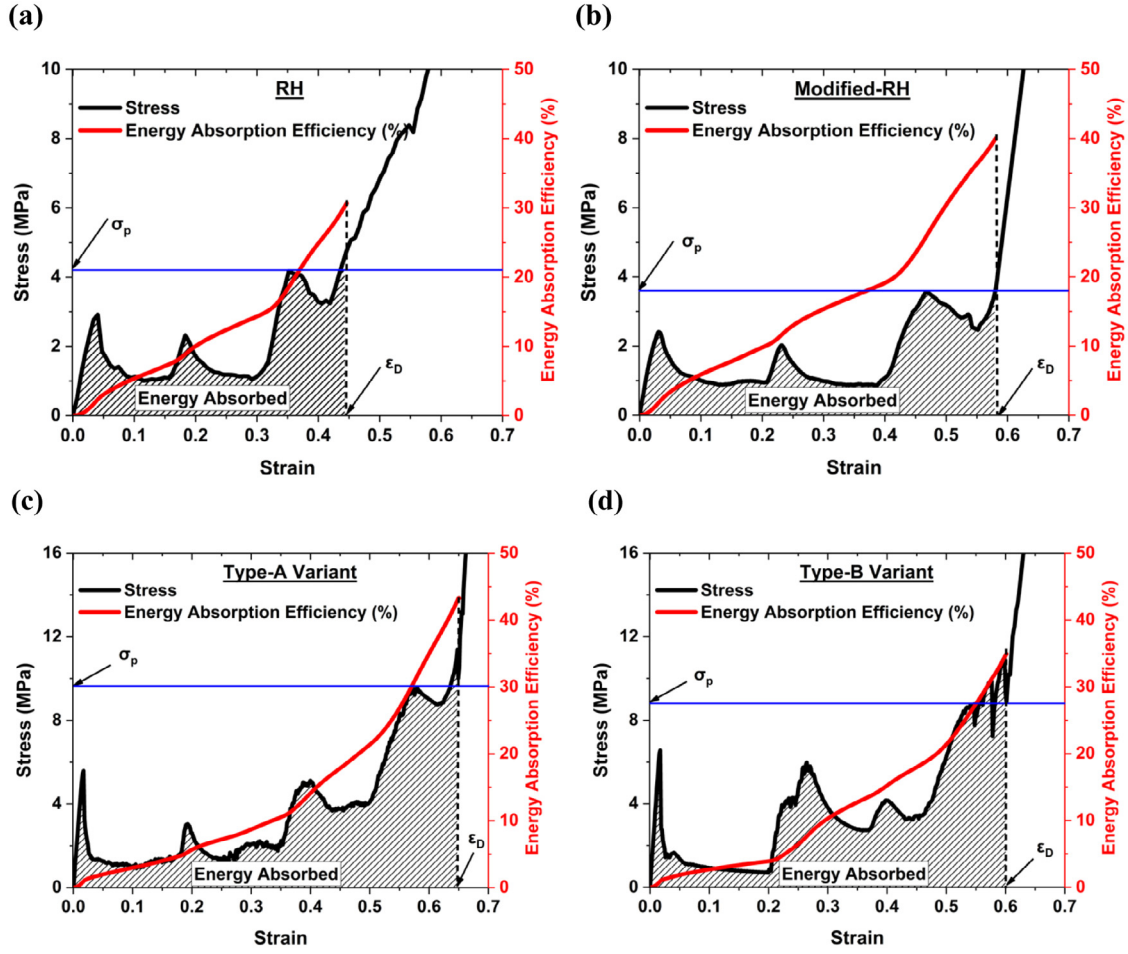
Fig. 10. Stress–strain response and energy absorption efficiency variation with strain: (a) RH, (b) Modified-RH, (c) Type-A variant and (d) Type-B variant. (For interpretation of the references to colour in this figure legend, the reader is referred to the web version of this article.)
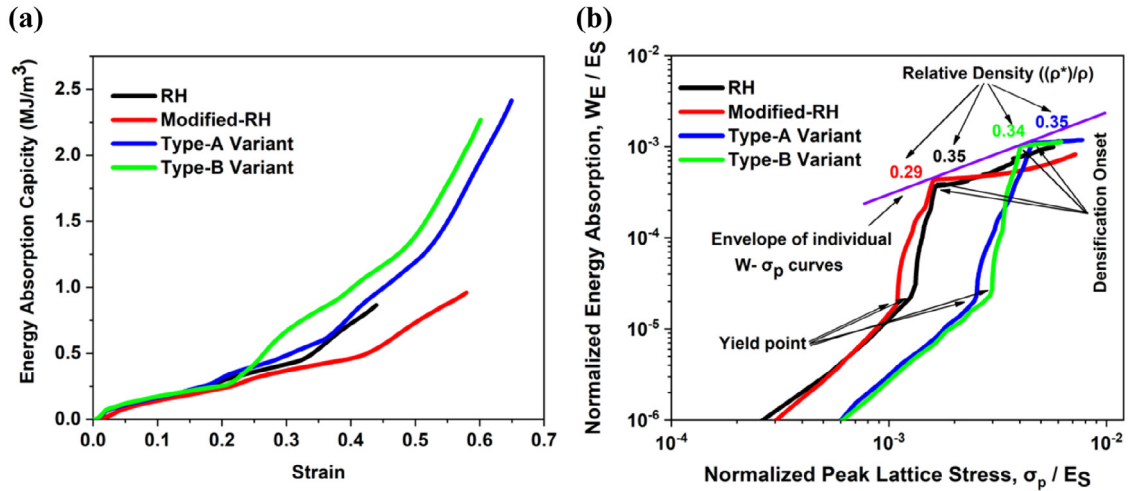

Fig. 11. Mechanical properties of RH, Modified-RH, Type-A variant and Type-B variant structures under quasi-static compression: (a) energy absorption capacity (b) normalized energy absorption plot, showing the envelope curve, the plastic yielding and densification onset points corresponding to the plateau region in the stress–strain curve.

structure to its density (ρ). SEA of the structures is calculated by using Eq. (25) [34].

$$SEA = \frac{1}{\rho} \int_0^{\varepsilon_D} \sigma(\varepsilon)\, d\varepsilon \qquad (25)$$

It is clear from Table 6 that the SEA of Type-A variant is the highest (6079.84 J/kg) among all the structures. The SEA of Type-B variant,

modified-RH and RH are found to be 5870.23 J/kg, 2816.47 J/kg and 2179.25 J/kg respectively. The highest improvement in SEA was seen for Type-A variant (178.98%) followed by Type-B variant (169.37%) when compared with RH structure. Similarly, with respect to modified-RH, Type-A and Type-B variants have 115.87% and 108.42% higher SEA capability respectively.

Table 6
Energy absorption response of structures.

| Structure	Energy absorption capacity (MJ/m³)			Specific energy absorption (J/kg)			Energy absorption efficiency (%)		
	Exp.	FEA	Error (%)	Exp.	FEA	Error (%)	Exp.	FEA	Error (%)
RH	0.701	0.739	5.142	2179.25	2332.06	7.01	28.98	30.66	5.79
Modified-RH	0.912	0.962	5.497	2816.47	2994.23	6.311	37.45	39.85	6.41
Type-A variant	2.217	2.412	8.784	6079.84	6651.97	9.41	40.27	43.27	7.45
Type-B variant	2.057	2.263	10.01	5870.23	6395.85	8.95	31.95	34.93	9.99
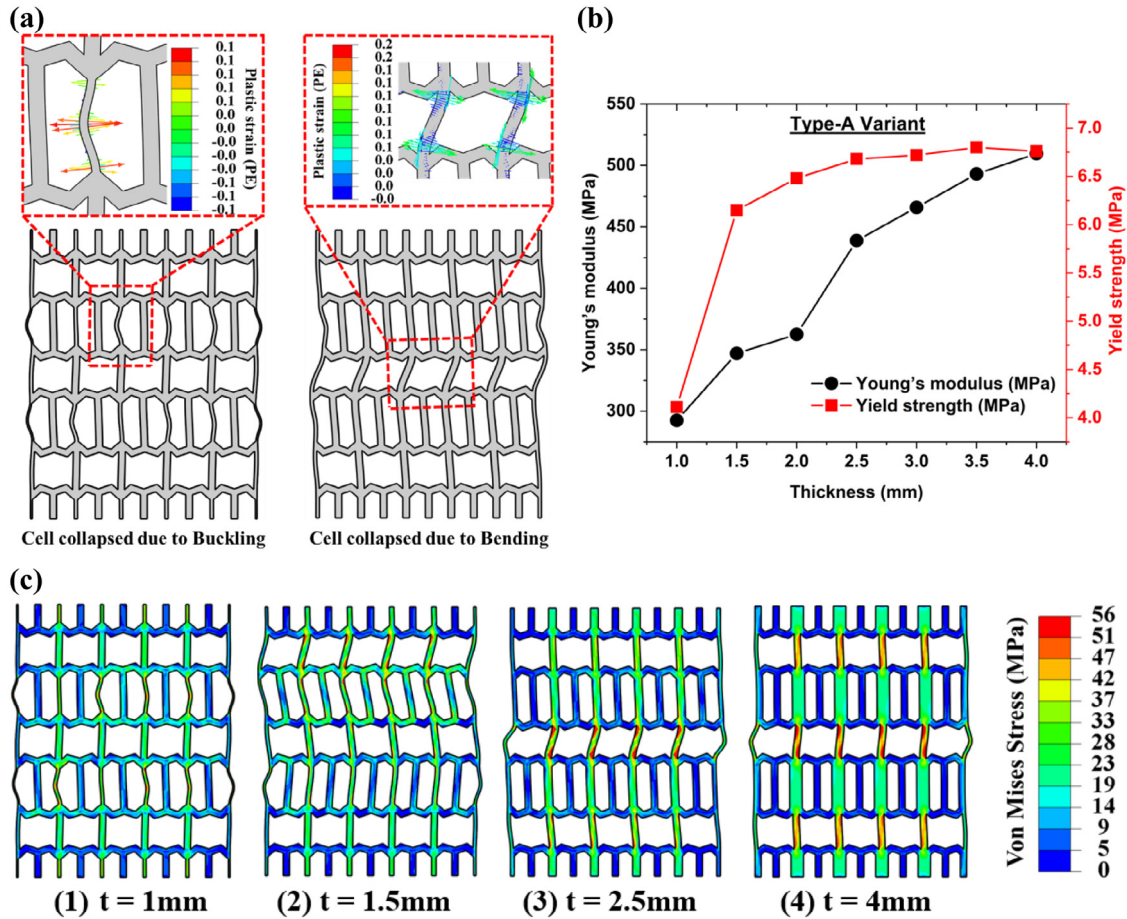
Fig. 12. Effect of vertical strut thickness on (a) cell collapse mechanism, (b) Young's modulus and yield strength and (c) deformation maps with Von Mises stress distribution at yield strain.

Despite having same relative density, energy absorption efficiencies of Type-A and Type-B variants are higher than RH structure by 41.12% and 13.93% respectively. Type-A variant has the highest energy absorption efficiency (43.27%) among all the four designs and more details about their deformation behavior can found in Section 4.4.1.

The normalized cumulative energy absorption versus peak stress plots for all lattice structures is presented in Fig. 11, following Gibson and Ashby et al. approach. Normalization of cumulative energy absorption and peak stress was done by dividing Young's modulus of the ABS material. Envelop is drawn at the best choice for a given maximum allowable stress (σ_P) of each structure, which relates energy absorption capacity (W_E) to the maximum allowable stress (σ_P).

At normalized peak lattice stress smaller than 0.003, the Type-A and Type-B variant structures undergo deformation within the elastic regime, while RH and modified-RH structures exhibit inelastic deformation and hence have higher normalized energy absorption than Type-A and Type-B variants. Since inelastic regimes of the Type-A and Type-B variants are much higher than those of the RH and modified-RH structures, therefore they exhibit better performance in terms of total energy absorption.

4.5. Parametric analysis: The effect of vertical strut thickness

In this section, the effect of wall thickness variation of the added vertical strut on the performance of Type-A variant lattice structure was studied. The numerical model was used to study the influence of thickness, t, which varies from 1 mm to 4 mm on the mechanical response of the structure. Despite slight mismatch between experimental and numerical results post-yield, it is expected that the parametric investigation can provide useful information for designing optimal lattice structures.

4.5.1. Young's modulus and yield strength

The cell collapse behavior of classical re-entrant honeycomb structure having variation in thickness of the walls is highly influenced by the weaker wall [52,53] and therefore, it was observed that the Type-A variants starts deforming plastically at the end of elastic regime. The behavior of the elastic regime is governed by the weaker wall of the cell as shown in Fig. 12(a).

Fig. 12(b) shows the variation of Young's modulus and yield strength of Type-A variants with respect to different strut thickness
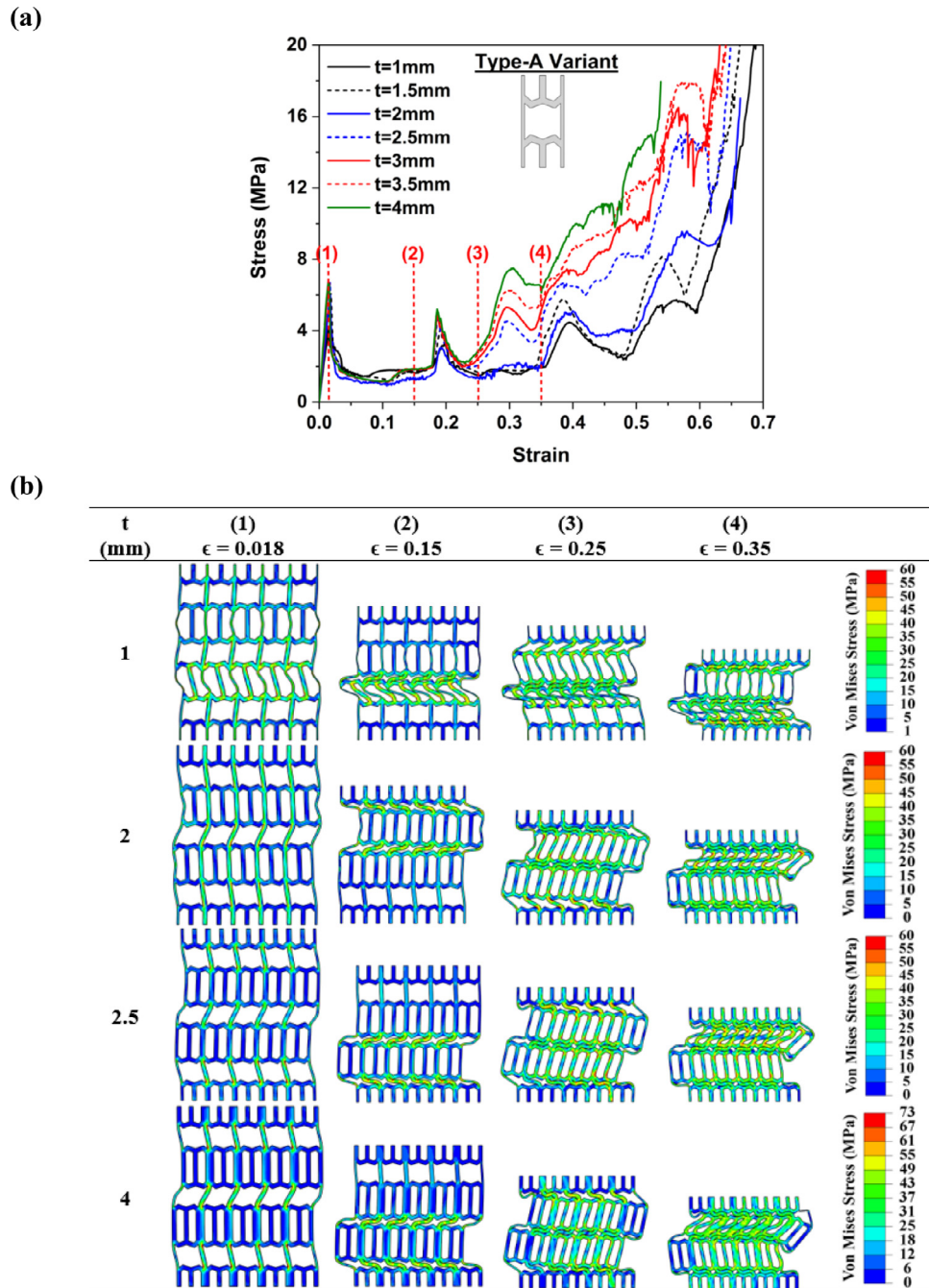
(a)

(b)

Fig. 13. Effect of added vertical strut thickness (t) for Type-A variant on (a) stress–strain response during quasi-static compression and (b) deformation sequences at different strains are correspondingly highlighted in the stress–strain curve.

't'. For 1 mm strut thickness, the structure showed very low value of Young's modulus (292.5 MPa) and yield strength (4.11 MPa) as the cell collapsed due to buckling of thinner vertical strut (Fig. 12(c)-(1)). Further increase in thickness to 1.5 mm, the collapse criteria changed from buckling to bending of the vertical members (Fig. 12(c)-(2)), and hence improvement was observed in both Young's modulus (347 MPa) and yield strength (6.15 MPa). The abrupt increase in the stiffness was observed when thickness increased from 2 mm to 2.5 mm. Before the bending occurs, axial component of the forces in the vertical wall contributes via axial yielding due to the short and squat wall [52]. This contribution results in higher stiffness which can be visualized by stress-bearing capacity of the elastically deforming vertical wall before plastic collapse (Fig. 12(c)-(3)). Further increase in thickness (to 4 mm) resulted in marginal improvement in Young's modulus and yield

strength values. Table 7 presents the mechanical properties of Type-A variants in relation to varied thickness (t) and relative density ($\bar{\rho}$).

4.5.2. Stress–strain response and energy absorption characteristics

Fig. 13(a) shows stress–strain response of the Type-A variant lattice structure for different strut thickness. Despite different peak stress intensities, the pattern of peak and valley formation within the plateau regime was found to be similar as thickness increased from 1 mm to 4 mm. Fig. 13(a) is marked with numbers 1 to 4 to understand the localized deformation behavior of the structure in different rows of unit cells as the failure of lattice structure is localized and the crush bands percolate throughout the lattice with increase in strain. The point-1 represents the end of elastic regime and after point-1, the cells deform plastically giving a long plateau before reaching the densification. The

Table 7
Mechanical properties of Type-A variant.

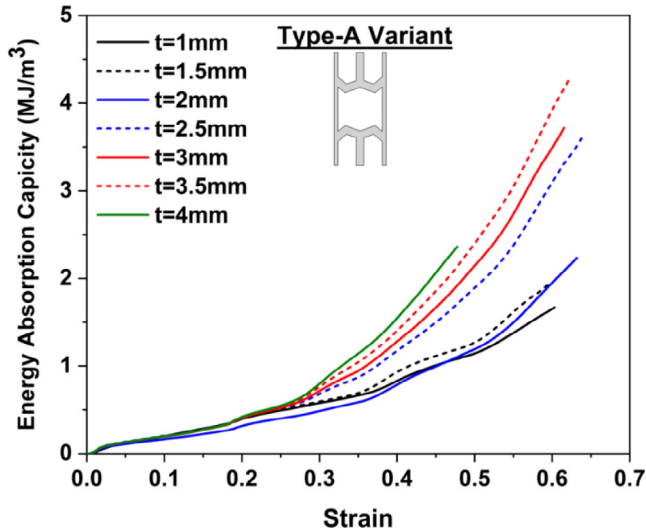| Properties	Thickness 't' (mm)						
	1	1.5	2	2.5	3	3.5	4
Young's modulus (MPa)	292.5	347	362.53	438.8	465.8	493	509.6
Yield strength (MPa)	4.11	6.15	6.48	6.68	6.72	6.80	6.76
$\bar{\rho}$	0.32	0.33	0.35	0.37	0.38	0.40	0.42

Fig. 14. Effect of variation of added vertical strut thickness (t) for Type-A variant structure on energy absorption capacity.

difference in deformation pattern can be seen for thickness of 1 mm, 2 mm and 2.5 mm and but after 2.5 mm, the deformation patterns are found to be similar (Fig. 13(b)).

Cell collapse occurred either due to the formation of plastic hinge at the location of the maximum moment within the strut or due to the buckling of the strut when the load increased to its critical buckling load (Euler buckling load).

When the thickness of added vertical strut is 1 mm the elastic behavior of the Type-A variant was determined by buckling of the thinner vertical strut (Fig. 13(b)-point-1), while the plastic behavior within the localized band was determined by both types of failure mode (buckling and bending) as can be seen in Fig. 13(b)-point-2 to 4. Load resistance in buckling is lower than that of bending and both are dependent on $\frac{t}{l}$ ratio of deforming strut. Since at t = 1 mm the load resistance during deformation by different vertical members was lower and hence lower stress response was obtained, which can be mapped with the Von Mises stress distribution within the deformed cells. An increase in thickness (to 2 mm) changes the cell collapse behavior and was completely dominated by failure due to bending (formation of a plastic hinge) (Fig. 13(b)). Further increase in thickness (2.5 mm to 4 mm) adds an axial component of load with bending in the vertical strut which improves its load resisting capacity (Fig. 13(b)-point-3 and 4).

Fig. 14 shows the variation of energy absorption capacity with strain. Initially, for strain up to 0.25, the energy absorption varies

linearly with strain, and the influence of added vertical strut thickness was negligible. As the strain increases, the energy absorption capacity increases exponentially since the deformation of lattices was controlled by sub-cell-2 which is highly influenced by thickness variation of the vertical strut. As thickness changes the total energy absorption capacity of the Type-A variant structure increases and reaches a maximum value for t = 3.5 mm. Further increase in thickness (i.e.4 mm) leads to early cell collapse and is responsible for low energy absorption (Fig. 13(a)). Due to increase in the thickness, the distance between the walls becomes lesser which leads to early failure (due to early percolation of contacts between cell walls) and hence reducing the onset of densification which ultimately reduces the total energy absorption.

Table 8 summarizes the energy absorption characteristics of the Type-A variant. It can be noted that the energy absorption capacity of the structure increased from 1.67 MJ/m³ to 4.29 MJ/m³ as thickness was increased from 1mm to 3.5 mm and reduced to 2.36 MJ/m³ for a thickness of 4mm. The maximum energy absorption capacity of the Type-A variant was observed for a thickness of 3.5 mm. Similar behavior was observed with the SEA of the structure. The SEA increased from 4975.47 J/kg to 10 230.02 J/kg as thickness increased from 1 mm to 3.5 mm and reduced to 5403.13 J/kg for a thickness of 4 mm. The influence of added vertical strut thickness on energy absorption efficiency is negligible and is between 30.73% to 33.99% for thickness of 1 mm to 3.5 mm except at 2.5 mm which showed the highest efficiency (43.27%). It is thus clear that the thickness of vertical strut highly influences the mechanical behavior of Type-A lattice structure. However, orientation of the struts with respect to loading also affects its loading capacity.

5. Conclusions

In this study, two novel re-entrant auxetic lattices namely, Type A and Type B variants were proposed by introducing vertical ligaments into conventional re-entrant lattice structure. Type A and Type B variants exhibit about 165% and 147% higher specific energy absorption than conventional re-entrant structure respectively, due to their effective composite architecture. Similarly, an improvement of about 355% and 198% in Young's modulus was observed for Type A and B auxetics respectively. The addition of ligament converts the unit cell into binary sub-cells and the resulting sub-cell properties were found to significantly affect the mechanical properties. The theoretical formulae for computing the effective Young's modulus of the proposed structures were developed using an energy-based approach and validated by the FE results. The FE model was able to reasonably accurately predict the deformation patterns and the failure observed in the experiments.

The Type A and B structures showed the highest energy absorption compared to re-entrant honeycomb (RH) structure which was due to deformation of higher relative density cells at higher strains. This was not observed in the conventional RH structure but the RH structure is more auxetic than Type-A and Type-B variants with a Poisson's ratio of −1.324, −0.121 and −0.057 respectively. The presence of vertical ligament in Type A and B structures restricted the inward movement of inclined walls, lowering the transverse strain and hence their Poisson's ratio. Architectural tailoring of auxetic structures opens the possibility of simultaneously enhancing stiffness, strength, and energy absorption. The enhanced stiffness and energy absorption capability make the

Table 8
Energy absorption characteristics of Type-A variant structure.

Properties	Thickness 't' (mm)						
	1	1.5	2	2.5	3	3.5	4
EA (MJ/m³)	1.67	1.94	2.41	3.60	3.72	4.29	2.36
SEA (J/kg)	4975.47	5534.63	6651.97	9366.27	9269.42	10 230.02	5403.13
η (%)	33.37	32.38	43.27	33.99	30.73	31.75	24.11
ε_D	0.60	0.60	0.63	0.64	0.62	0.62	0.48
$\bar{\rho}$	0.32	0.33	0.35	0.37	0.38	0.40	0.42

proposed novel structures as potential candidates for protective devices. However, the dynamic behavior needs to be studied for their potential use in impact energy absorbing applications.

CRediT authorship contribution statement

Niranjan Kumar Choudhry: Conceptualization, Methodology, Validation, Formal analysis, Investigation, Data curation, Writing – original draft. **Biranchi Panda:** Resources, Supervision, Writing – review & editing, Project administration. **S. Kumar:** Writing – review & editing.

Declaration of competing interest

The authors declare that they have no known competing financial interests or personal relationships that could have appeared to influence the work reported in this paper.

Data availability

Data will be made available on request.

Acknowledgment

Appendix A. Supplementary data

Supplementary material comprising details of experimental setup for quasi-static compression tests, material characterization, FE model and its constitutive description, FE mech convergence test, optical imaging of FDM printed structures, sub-cell analysis of Type A and B structures, scaling relationships for for Type-A and Type-B variants, and edge effects can be found online at https://doi.org/10.1016/j.tws.2023.110650.

References

[1] L.J. Gibson, M.F. Ashby, Cellular Solids: Structure and Properties, Cambridge University Press, 1999.

[2] J. Ubaid, J. Schneider, V.S. Deshpande, B.L. Wardle, S. Kumar, Multifunctionality of nanoengineered self-sensing lattices enabled by additive manufacturing, Adv. Eng. Mater. (2022).

[3] M.F. Arif, S. Kumar, T. Shah, Tunable morphology and its influence on electrical, thermal and mechanical properties of carbon nanostructure-buckypaper, Mater. Des. 101 (2016) 236–244.

[4] X.Y. Zhang, X. Ren, Y. Zhang, Y.M. Xie, A novel auxetic metamaterial with enhanced mechanical properties and tunable auxeticity, Thin-Walled Struct. 174 (2022) 109162, http://dx.doi.org/10.1016/j.tws.2022.109162.

[5] F. Alam, K.M. Varadarajan, J.H. Koo, B.L. Wardle, S. Kumar, Additively manufactured polyetheretherketone (PEEK) with carbon nanostructure reinforcement for biomedical structural applications, Adv. Eng. Mater. 22 (2020) 2000483.

[6] I. Yadroitsava, A. du Plessis, I. Yadroitsev, Bone Regeneration on Implants of Titanium Alloys Produced by Laser Powder Bed Fusion: A Review, Elsevier Inc., 2019, http://dx.doi.org/10.1016/B978-0-12-815820-3.00016-2.

[7] P. Verma, J. Ubaid, K.M. Varadarajan, B.L. Wardle, S. Kumar, Synthesis and characterization of carbon nanotube-doped thermoplastic nanocomposites for the additive manufacturing of self-sensing piezoresistive materials, ACS Appl. Mater. Interfaces 14 (2022) 8361–8372.

[8] J.J. Andrew, H. Alhashmi, A. Schiffer, S. Kumar, V.S. Deshpande, Energy absorption and self-sensing performance of 3D printed CF/PEEK cellular composites, Mater. Des. 208 (2021) 109863.

[9] J.J. Andrew, P. Verma, S. Kumar, Impact behavior of nanoengineered, 3D printed plate-lattices, Mater. Des. 202 (2021) 109516, http://dx.doi.org/10.1016/j.matdes.2021.109516.

[10] G. Imbalzano, S. Linforth, T.D. Ngo, P.V.S. Lee, P. Tran, Blast resistance of auxetic and honeycomb sandwich panels: Comparisons and parametric designs, Compos. Struct. 183 (2018) 242–261.

[11] G. Imbalzano, P. Tran, T.D. Ngo, P.V.S. Lee, A numerical study of auxetic composite panels under blast loadings, Compos. Struct. 135 (2016) 339–352.

[12] G. Imbalzano, P. Tran, T.D. Ngo, P.V.S. Lee, Three-dimensional modelling of auxetic sandwich panels for localised impact resistance, J. Sandw. Struct. Mater. 19 (2017) 291–316.

[13] T. Dixit, E. Al-Hajri, M.C. Paul, P. Nithiarasu, S. Kumar, High performance, microarchitected, compact heat exchanger enabled by 3D printing, Appl. Therm. Eng. 210 (2022) 118339.

[14] V. Gupta, F. Alam, P. Verma, A.M. Kannan, S. Kumar, Additive manufacturing enabled, microarchitected, hierarchically porous polylactic-acid/lithium iron phosphate/carbon nanotube nanocomposite electrodes for high performance Li-Ion batteries, J. Power Sources 494 (2021) 229625.

[15] S. Linforth, T. Ngo, P. Tran, D. Ruan, R. Odish, Investigation of the auxetic oval structure for energy absorption through quasi-static and dynamic experiments, Int. J. Impact Eng. 147 (2021) 103741, http://dx.doi.org/10.1016/j.ijimpeng.2020.103741.

[16] K.E. Evans, M.A. Nkansah, I.J. Hutchinson, S.C. Rogers, Molecular network design, Nature 353 (1991) 124.

[17] C. Mercer, T. Speck, J. Lee, D.S. Balint, M. Thielen, Effects of geometry and boundary constraint on the stiffness and negative Poisson's ratio behaviour of auxetic metamaterials under quasi-static and impact loading, Int. J. Impact Eng. 169 (2022) 104315, http://dx.doi.org/10.1016/j.ijimpeng.2022.104315.

[18] L. Kai, C. Xiaofei, Z. Peng, W. WenWang, L. Ying, Dynamic mechanical performances of enhanced anti-tetra-chiral structure with rolled cross-section ligaments under impact loading, Int. J. Impact Eng. 166 (2022) 104204, http://dx.doi.org/10.1016/j.ijimpeng.2022.104204.

[19] L.L. Hu, Z.R. Luo, Q.Y. Yin, Negative Poisson's ratio effect of re-entrant anti-trichiral honeycombs under large deformation, Thin-Walled Struct. 141 (2019) 283–292, http://dx.doi.org/10.1016/j.tws.2019.04.032.

[20] X. Zhang, R. Tian, Z. Zhang, G. Li, W. Feng, In-plane elasticity of a novel vertical strut combined re-entrant honeycomb structure with negative Poisson's ratio, Thin-Walled Struct. 163 (2021) 107634, http://dx.doi.org/10.1016/j.tws.2021.107634.

[21] R. Lakes, Foam structures with a negative Poisson's ratio, Science (80-) 235 (1987) 1038–1041.

[22] Y. Sun, N.M. Pugno, In plane stiffness of multifunctional hierarchical honeycombs with negative Poisson's ratio sub-structures, Compos. Struct. 106 (2013) 681–689, http://dx.doi.org/10.1016/j.compstruct.2013.05.008.

[23] D. Rayneau-Kirkhope, Stiff auxetics: Hierarchy as a route to stiff, strong lattice based auxetic meta-materials, Sci. Rep. 8 (2018) 1–10, http://dx.doi.org/10.1038/s41598-018-30822-x.

[24] K. Zied, M. Osman, T. Elmahdy, Enhancement of the in-plane stiffness of the hexagonal re-entrant auxetic honeycomb cores, Phys. Status Solidi Basic Res. 252 (2015) 2685–2692, http://dx.doi.org/10.1002/pssb.201552164.

[25] Z.X. Lu, X. Li, Z.Y. Yang, F. Xie, Novel structure with negative Poisson's ratio and enhanced Young's modulus, Compos. Struct. 138 (2016) 243–252, http://dx.doi.org/10.1016/j.compstruct.2015.11.036.

[26] Z. Chen, X. Wu, Y.M. Xie, Z. Wang, S. Zhou, Re-entrant auxetic lattices with enhanced stiffness: A numerical study, Int. J. Mech. Sci. 178 (2020) http://dx.doi.org/10.1016/j.ijmecsci.2020.105619.

[27] M.H. Fu, Y. Chen, L.L. Hu, A novel auxetic honeycomb with enhanced in-plane stiffness and buckling strength, Compos. Struct. 160 (2017) 574–585, http://dx.doi.org/10.1016/j.compstruct.2016.10.090.

[28] M.-H. Fu, Y. Chen, L.-L. Hu, Bilinear elastic characteristic of enhanced auxetic honeycombs, Compos. Struct. 175 (2017) 101–110.

[29] W. Zhang, S. Zhao, F. Scarpa, J. Wang, R. Sun, In-plane mechanical behavior of novel auxetic hybrid metamaterials, Thin-Walled Struct. 159 (2021) http://dx.doi.org/10.1016/j.tws.2020.107191.

[30] A. Ingrole, A. Hao, R. Liang, Design and modeling of auxetic and hybrid honeycomb structures for in-plane property enhancement, Mater. Des. 117 (2017) 72–83, http://dx.doi.org/10.1016/j.matdes.2016.12.067.

[31] V.S. Deshpande, N.A. Fleck, Isotropic constitutive models for metallic foams, J. Mech. Phys. Solids 48 (2000) 1253–1283.

[32] N. Karathanasopoulos, H. Reda, J. francois Ganghoffer, Designing two-dimensional metamaterials of controlled static and dynamic properties, Comput. Mater. Sci. 138 (2017) 323–332, http://dx.doi.org/10.1016/j.commatsci.2017.06.035.

[33] V.S. Deshpande, M.F. Ashby, N.A. Fleck, Foam topology: Bending versus stretching dominated architectures, Acta Mater. 49 (2001) 1035–1040, http://dx.doi.org/10.1016/S1359-6454(00)00379-7.

[34] N.K. Choudhry, B. Panda, S. Kumar, In-plane energy absorption characteristics of a modified re-entrant auxetic structure fabricated via 3D printing, Composites B 228 (2022) 109437.

[35] Y. Zhu, Y. Luo, D. Gao, C. Yu, X. Ren, C. Zhang, In-plane elastic properties of a novel re-entrant auxetic honeycomb with zigzag inclined ligaments, Eng. Struct. 268 (2022) 114788, http://dx.doi.org/10.1016/j.engstruct.2022.114788.

[36] A. Alomarah, S.H. Masood, D. Ruan, Out-of-plane and in-plane compression of additively manufactured auxetic structures, Aerosp. Sci. Technol. 106 (2020) 106107, http://dx.doi.org/10.1016/j.ast.2020.106107.

[37] N.K. Choudhry, S.R. Bankar, B. Panda, H. Singh, Experimental and numerical analysis of the bending behavior of 3D printed modified auxetic sandwich structures, Mater. Today Proc. 56 (2022) 1356–1363.

[38] Y. Tao, F. Kong, Z. Li, J. Zhang, X. Zhao, Q. Yin, et al., A review on voids of 3D printed parts by fused filament fabrication, J. Mater. Res. Technol. 15 (2021) 4860–4879, http://dx.doi.org/10.1016/j.jmrt.2021.10.108.

[39] L.G. Blok, M.L. Longana, H. Yu, B.K.S. Woods, An investigation into 3D printing of fibre reinforced thermoplastic composites, Addit. Manuf. 22 (2018) 176–186, http://dx.doi.org/10.1016/j.addma.2018.04.039.

[40] F. Alam, P. Verma, W. Mohammad, J. Teo, K.M. Varadarajan, S. Kumar, Architected poly (lactic acid)/poly (ε-caprolactone)/halloysite nanotube composite scaffolds enabled by 3D printing for biomedical applications, J. Mater. Sci. 56 (2021) 14070–14083.

[41] K.P. Logakannan, D. Ruan, J. Rengaswamy, S. Kumar, V. Ramachandran, Fracture locus of additively manufactured AlSi10Mg alloy, Thin-Walled Struct. 184 (2023) 110460.

[42] M.F. Ashby, The properties of foams and lattices, Philos. Trans. R. Soc. A Math. Phys. Eng. Sci. 364 (2006) 15–30.

[43] T. Maconachie, M. Leary, B. Lozanovski, X. Zhang, M. Qian, O. Faruque, et al., SLM lattice structures: Properties, performance, applications and challenges, Mater. Des. 183 (2019) 108137.

[44] H. Wang, P. Chen, H. Wu, A. Chen, S. Wu, J. Su, et al., Comparative evaluation of printability and compression properties of poly-ether-ether-ketone triply periodic minimal surface scaffolds fabricated by laser powder bed fusion, Addit. Manuf. (2022) 102961.

[45] A. Alomarah, S.H. Masood, I. Sbarski, B. Faisal, Z. Gao, D. Ruan, Compressive properties of 3D printed auxetic structures: experimental and numerical studies, Virtual Phys. Prototyp. 15 (2020) 1–21.

[46] H. Lu, X. Wang, T. Chen, In-plane dynamics crushing of a combined auxetic honeycomb with negative Poisson's ratio and enhanced energy absorption, Thin-Walled Struct. 160 (2021) 107366.

[47] A. Harkati, D. Boutagouga, E. Harkati, A. Bezazi, F. Scarpa, M. Ouisse, In-plane elastic constants of a new curved cell walls honeycomb concept, Thin-Walled Struct. 149 (2020) http://dx.doi.org/10.1016/j.tws.2020.106613.

[48] M.S. Saleh, C. Hu, J. Brenneman, A.M. Al Mutairi, R. Panat, 3D printed three-dimensional metallic microlattices with controlled and tunable mechanical properties, Addit. Manuf. 39 (2021) 101856, http://dx.doi.org/10.1016/j.addma.2021.101856.

[49] F. Yi, Z. Zhu, F. Zu, S. Hu, P. Yi, Strain rate effects on the compressive property and the energy-absorbing capacity of aluminum alloy foams, Mater. Charact. 47 (2001) 417–422, http://dx.doi.org/10.1016/S1044-5803(02)00194-8.

[50] L. Cui, S. Kiernan, M.D. Gilchrist, Designing the energy absorption capacity of functionally graded foam materials, Mater. Sci. Eng. A 507 (2009) 215–225, http://dx.doi.org/10.1016/j.msea.2008.12.011.

[51] Q.M. Li, I. Magkiriadis, J.J. Harrigan, Compressive strain at the onset of densification of cellular solids, J. Cell. Plast. 42 (2006) 371–392.

[52] L.J. Gibson, M.F. Ashby, Lorna J. Gibson, Michael F. Ashby, Cellular Solid(z-lib.org).pdf, in: Cambridge Solid State Sci Ser, 1997.

[53] C. Quan, B. Han, Z. Hou, Q. Zhang, X. Tian, T.J. Lu, 3D printed continuous fiber reinforced composite auxetic honeycomb structures, Composites B 187 (2020) http://dx.doi.org/10.1016/j.compositesb.2020.107858.